AIAA JOURNAL
Vol. 39, No. 10, October 2001

Performance of a Titan Rocket Engine Using Laser-Induced Fluorescence of OH

L. M. Cohen,* D. M. Jassowski,† and J. I. Ito‡
Aerojet, Sacramento, California 95813-6000

Rocket engine performance can be modeled by considering separately the propellant delivery system distribution, combustion efficiency including propellant vaporization and gas-phase mixing, and nozzle expansion efficiency. Although these quantities can be modeled, experimental verification is extremely helpful for separately understanding these processes and for design improvements. Laser-induced fluorescence of OH, excited by a KrF excimer laser operating at 248 nm, is used to measure the concentration of the OH radical across the exit plane of a firing Titan IV, stage I, liquid rocket engine, from which the combusting mixture ratio profile could be inferred. These measurements allow assessment of the degree of mixing and potential flow stratification between the injector core, combustion baffles, and combustion chamber fuel-film cooling and can help to provide the basis for future performance optimization.

Nomenclature

A	=	Einstein A coefficient
Aa	=	area of the laser beam (height times thickness)
B_{12}	=	Einstein second coefficient for stimulated absorption
c	=	speed of light
E	=	laser energy per pulse
$f_B(T)$	=	temperature-dependent Boltzmann fraction of the absorbing state
$g(\nu)$	=	spectral overlap function
$h\nu$	=	energy of a scattered photon
K	=	non-noise-free gain factor
M	=	magnification of the imaging system
N_c	=	number of counts recorded by the camera per pixel
N_p	=	number of laser pulses integrated
N_T	=	total number density of the gas
P_c	=	rocket engine combustion chamber pressure
Q_{pre}	=	predissociation rate
S	=	fluorescence signal
T	=	gas temperature
u_{radial}	=	radial component of the velocity
V	=	collection volume
η	=	collection efficiency
χ_{OH}	=	mole fraction of OH
Ω	=	collection solid angle per pixel
ω	=	wave number of the laser

Subscript

pp	=	per pixel

Introduction

THE Titan IV, stage I engine is a large, 2.446×10^6 N (nominal) thrust (vacuum), booster engine that uses Aerozine-50 fuel (a 50/50 weight mixture of hydrazine and unsymmetrical-dimethylhydrazine) and nitrogen tetroxide oxidizer as the storable propellants flowing at 816 kg/s in a pump-fed, gas generator cycle. The engine is robust and highly reliable, never having experienced a failure during over 200 of its 190-s flight missions. The thrust is generated by two nearly identical thrust chamber subassemblies, one of which was probed by the laser. The combustion chamber pressure is 5.86×10^6 N/m^2 (nominal). The combustion chamber was fuel regeneratively cooled and had a 6:1 area ratio nozzle with an exit diameter (inside) of 0.95 m (without an ablative skirt). All measurements were performed at the nozzle exit plane.

Nonuniform mixing of the fuel and oxidizer streams in a rocket engine may lead to regions of varying mixture ratio (MR), the ratio of the oxidizer to fuel mass flow rates. Engine performance as measured by the specific impulse I_{sp} depends on the MR.[1] Wherever the MR is not at the optimum value, there is a penalty paid in reduced I_{sp}. The purpose of this work was to use laser measurements of the spatially varying MR to determine if there were sufficient regions of nonuniform MR in the exhaust plane of the engine to merit an injector modification for recovering this lost I_{sp}. Fuel is used as a film coolant for the walls of the combustion chamber and nozzle. The overall MR includes the fuel film coolant, whereas the core MR does not. The stoichiometric MR is 2.25.

Optical diagnostics are ideally suited for making gas concentration measurements in hostile combustion environments because they provide nonintrusive access to the flow. Laser-induced fluorescence is probably the most well-known technique for radical species measurements, having been used extensively since the early 1980s. It provides high spatial resolution (typically 0.1 mm), high temporal resolution (typically less than 100 ns), and high sensitivity (typically concentrations in the parts per million range).

The specific technique used was laser-induced fluorescence (LIF) of the naturally occurring OH combustion radical in the exhaust plume. A KrF excimer laser (248 nm) was used to excite the OH molecules to minimize the dependence of the resulting fluorescence on quenching and to maximize the predissociation-dominated decay process. Predissociation occurs when the potential energy curve for a bound molecular state is crossed by the curve of a repulsive, that is, unbound, state. When this particular LIF approach was chosen, the measurements were specifically sensitive to the OH concentration in the flow. Other researchers have also used laser techniques to make spatially resolved measurements in rocket plumes. LIF of sodium has been used to measure the temperature, velocity and fluorescence intensity in the shuttle orbital maneuvering subsystem engine (amine fuel and nitrogen tetroxide oxidizer).[2] LIF and Raman spectroscopy in a small (7.37-cm-diam exit plane) liquid rocket engine (mixed-amines fuel and red fuming nitric acid oxidizer) were used to measure temperature and water concentration.[3] The measurements reported here are a valuable, new contribution to the field because of the much larger scale of this engine and the significance of measuring the important, MR-sensitive, OH radical.

The laser beam was swept across the engine at the exit plane, in discrete increments, to probe the flowfield at different locations

Presented as Paper 99-2169 at the AIAA/ASME/SAE/ASEE 35th Joint Propulsion Conference, Los Angeles, CA, 20–24 June 1999; received 27 July 1999; revision received 1 March 2001; accepted for publication 13 March 2001.

*Engineering Specialist; currently Project Manager, Telecommunications, Coherent, 2303 Lindbergh St., Auburn, CA 95602; larry.cohen@coherentinc.com. Senior Member AIAA.

†Engineering Specialist; currently President, JEM Industries, P.O. Box 3069, Diamond Springs, CA 95619. Member AIAA.

‡Technical Principal; currently Consultant.

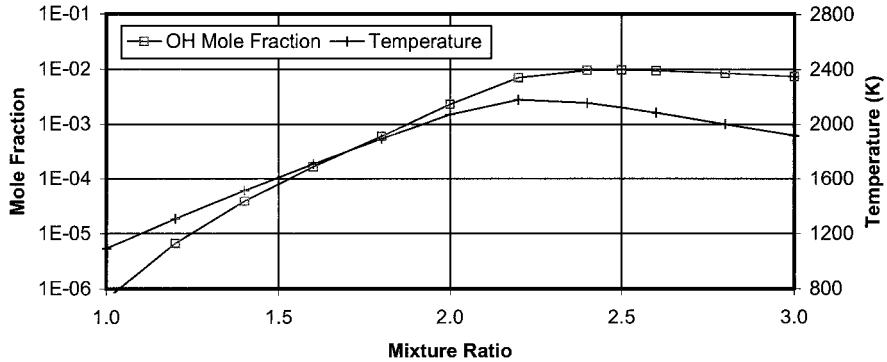

Fig. 1 ODK predictions for OH mole fraction and temperature of the exhaust gases for the Titan IV, stage I, engine at $A/A^* = 6$ ($P_c = 5.91 \times 10^6$ N/m^2).

and times. An intensified charge-coupled device (CCD) camera monitored the fluorescence along the beam path. Kinetics models were used to relate the OH concentration to the local propellant MR. The shape of the OH profile will depend on the hydraulic distribution caused by the oxidizer dome, the combustion-stabilizing baffles near the injector, and by the engine operating conditions (combustion chamber pressure and overall MR). The results show that the OH profile (and, therefore, MR distribution) is not radially symmetric.

Technical Discussion

Figure 1 shows the results of a One-Dimensional Kinetics (ODK) code[4] calculation at the engine exit conditions, which indicates that, over a wide range, the OH molecule is a sensitive marker of MR (i.e., its concentration changes significantly with changes in MR) up to about an MR of 2.3. The MR region of interest for the engine tests to be reported here is from 1.2 to 2.5, or temperatures between 1300 and 2100 K and OH mole fractions between 7 and 9800 ppm. The Two-Dimensional Kinetics (TDK) code[4] was used to predict the shape of the OH mole fraction profile at the exit plane ($A/A^* = 6$, exit diameter = 0.95 m). In a one-zone approximation to the flowfield, the barrier film cooling was ignored and OH mole fractions were calculated for core MR values of 1.1–2.5. Except at very low MR, the OH profile was essentially flat. This is fortuitous because it implies that observed changes in the OH concentration across the engine must indicate changes in MR.

We used nonsaturated, optically thin, planar laser-induced predissociative fluorescence (PLIPF) as the laser technique. The governing equation for this process is

$$S_{\text{pp}} = \eta(\Omega/4\pi)(B_{12}/c)(EN_p/Aa)V_{\text{pp}}(A/Q_{\text{pre}})\chi_{\text{OH}}N_T f_B(T)g(\nu) \tag{1}$$

Note that S_{pp} is the measured quantity of the fluorescence signal from a single CCD camera frame (multiple laser shots). Also, η is a lumped efficiency that includes three factors: the transmission efficiency of the collection lenses and filters, the camera's photocathode quantum efficiency, and the electronic gain of the camera system (in counts per photoelectron). The total number of pulses integrated per image acquired, N_p, is the laser repetition rate times the camera exposure time. The Stern–Vollmer factor (or fluorescence efficiency) is A divided by Q_{pre}. The spectral overlap function $g(\nu)$ is the convolution of the Gaussian laser and the Voigt absorption line.

In these experiments, the $Q_2(11)$ absorption line of OH was excited at 248 nm [$A^2\Sigma^+(\nu' = 3) \leftarrow X^2\Pi(\nu'' = 0)$] and detected at 297 nm [$A^2\Sigma^+(\nu' = 3) \rightarrow X^2\Pi(\nu'' = 2)$]. Although the strength of this OH transition is lower than others that could be used, for example, at 284 or 308 nm, the advantages (reduced absorption of the laser across the flow and quench rate independence) make this the proper excitation strategy for this flowfield.[5,6] This approach has been used before, for example, to measure OH in the cylinder of an automobile engine[7] and in a laboratory-scale, supersonic, H_2–air combustion tunnel.[8]

For a given experimental setup and OH absorption line, there are many terms in Eq. (1) that are constants. Then, Eq. (1) can be rewritten to show only the dependence on flowfield properties as

$$S_{\text{pp}} \propto \chi_{\text{OH}} P[f_B(T)/T] \tag{2}$$

where the temperature dependence is lumped into the term in brackets. The equation clearly shows the linear dependence of the fluorescence signal on the mole fraction of OH, the static pressure, and the static temperature. Within the tuning range of the KrF excimer laser, there are many OH absorption lines from the (3,0) vibrational band of the A–X electronic system.[9] We minimized the temperature dependence by picking a rotational level such that the quantity $f_{Br}(T)/T$, in Eq. (2), does not vary over the temperature range of interest. Over the expected temperature range of 1300–2100 K, the rotational f_{Br}, vibrational f_{Bv}, and electronic f_{Be} populations have relatively flat behavior, varying only by ±5% about the mean value. Because of this minimum temperature sensitivity and because good separation between rotational lines is desirable from an experimental standpoint, we chose to probe the $Q_2(11)$ absorption line.

The excimer laser output has both a narrowband (approximately 0.55 cm^{-1} or 0.003 nm, as measured with an etalon) and a broadband (approximately 0.5–0.8 nm) component; nominally, about 95% of the laser's energy is contained in the narrowband portion. The narrowband component is what selectively excites the OH absorption line, whereas the broadband part excites all of the species and lines that exist within the bandwidth of the laser. This includes lines for O_2, H_2O, and OH. When the laser is tuned to the center of the selected OH line (on-peak), the resulting fluorescence is in part due to the particular OH line and in part due to fluorescence from other OH lines and other species that are simultaneously excited with the broadband component. To isolate only the particular OH fluorescence of interest, the laser is tuned off-peak to the wing of the absorption line. The off-peak, or background, fluorescence is subtracted from the on-peak measurement to obtain the signal of interest.

The limiting values of MR expected in the flow ranged from 1.3, in the film-cooling region near the wall during the low MR test, to 2.3, in the core of the flow during the high MR test (see Table 1). (Later, these MR values are used to calculate the expected range of temperature and pressure in the flowfield.) The absorption linewidth depends on Doppler, pressure, and predissociation broadening. These linewidths, presented as full widths at half-maximum (FWHM in cm^{-1}) were taken as 0.27–0.34 for Doppler broadening (over the range of 1500–2300 K); 0.04–0.07 for pressure broadening (between 1500 K, 1.02 atm and 2300 K, 2.04 atm) using $\Delta\omega_c = 0.1(P, \text{ atm})(273/T)^{0.5}$ cm^{-1}; and 0.05 for predissociative broadening[10] (or $Q_{\text{pre}} = 1.33 \times 10^{10}\text{s}^{-1}$) to give the widest range of calculated broadening values. The combined Voigt line shape had a FWHM of 0.33–0.41 cm^{-1}. Convolving these values with the 0.55-cm^{-1} laser bandwidth gave an effective linewidth of 0.67–0.72 cm^{-1}. Therefore, over the range of flowfield conditions, the overlap function was approximately constant as 1.272 cm.

Experimental Arrangement

Aerojet's Mobile Diagnostics Laboratory (MDL) is a trans-oceanic cargo container that has been modified for laser diagnostics applications. It is equipped with full electric utilities (110 V, 220 V), air conditioning, specialized gas storage, and analog and digital communication lines to the engine test stand and the control

Table 1 Rocket engine, laser and ICCD camera test conditions

Test date	Test	Laser wavelength	Laser position scanned	Titan engine test condition	P_c, psia	Thrust chamber MR	Core MR	Average laser energy, mJ/pulse	Exposure, s	Laser pulses (at 80 Hz)
26 Jan. 1996	1	On-peak	Yes	Baseline	831	1.98	2.20	101	1.00	80
7 March 1996	2	On-peak; off-peak	No	High power	869	1.83	2.03	180	0.50	40
17 April 1996	3	On-peak; off-peak	Yes	High temperature	827	2.09	2.32	185	0.15	12

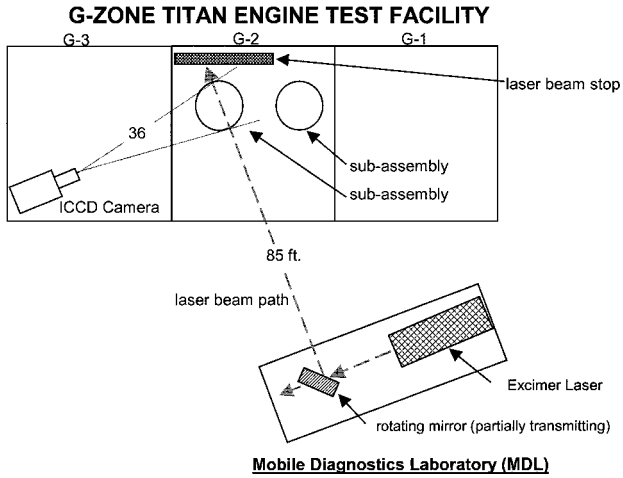

Fig. 2 Plan view of the G-zone test stand showing the location of the MDL and laser beam path.

room. For these tests, it was installed on the Aerojet G-zone (Titan engine) test stand apron, about 25.9 m from the engine, as shown schematically in Fig. 2. Note that the laser beam is shown at its nominal position, crossing subassembly 2 at the diameter (which corresponds to the center of the plume).

Installed in the MDL were the excimer laser system, the beam optics, the reference burner (to be discussed), a photomultiplier tube (PMT) for monitoring the LIF signal, electronics for laser sequencing, laser tuning, and beam steering, three computers, and a data acquisition system. The remotely controlled micrometer attached to the grating mount of the laser oscillator permitted scans and fine tuning of the laser wavelength.

A Lambda-Physik 150T MSC tunable excimer laser was used as the excitation light source; operating with KrF gas, the output wavelength was 248 nm. The laser was operated at up to 80 pulses/s with pulse energies as high as 200 mJ/pulse. The laser pulse width was 40 ns, fast enough to freeze flows traveling at 5 km/s.

A laboratory-standard, flat flame McKenna burner, running on methane–air and utilizing a shroud flow of nitrogen, was used to obtain a well-defined region of postflame gases, specifically hot OH. Part of the laser beam crossed through the postflame gases. The resulting fluorescence, monitored at right angles with a PMT, was used for tuning the laser wavelength to the center of the $Q_2(11)$ absorption line. [The same filters were used in front of the PMT and the intensified CCD (ICCD) camera lens.] The output from the PMT was measured with a gated integrator (boxcar averager) having a gate width of 150 ns.

The laser beam was directed through a port in the wall of the MDL and toward the engine with a 90 deg turning mirror mounted on a motorized, remotely controlled rotation stage. The stage position was controlled with vendor-supplied software and a dedicated personal computer. The laser wavelength was remotely controlled by adjusting the position of the grating at the end of the oscillator cavity with a digital stepper motor. The motor was controlled with vendor-supplied software and a dedicated personal computer.

Five different paths (chords) across the engine could be probed by directing the turning mirror in the MDL to preprogrammed settings. These five positions were (refer to Fig. 3a) 1) engine diameter (i.e., through the engine centerline), and then parallel to that position but with the beam moved 2) north by one-half of the engine radius, 3) north by 0.85 of the engine radius, 4) south by one-half of the radius, and 5) south by 0.85 radius. The laser beam started at position 1, and stayed there for 6 s, before scanning to position 2 (staying there for 3 s), position 3 (for 3 s), back to 1 (6 s), over to 4 (3 s) and 5 (3 s) before returning to 1 (and repeating the cycle once more). A strip of thermal burn paper stretched across the (nonfiring) engine exit, normal to the beam path, recorded the beam positions as burn patterns on the paper.

Figure 3b shows the orientation of the laser beam (as seen from below) with respect to the engine geometry: oxidizer inlet, injector elements, and combustion baffles. Note that some of the laser beams enter the engine plume near the oxidizer inlet and that the laser beams cross under or near most of the combustion baffles. Figure 3c is a schematic showing details of the oxidizer inlet. From the inlet, the oxidizer travels over each pie-shaped cover before flowing down into the adjacent radial channels in the injector. Figure 3d is a detailed schematic of the combustion baffles (as seen from below). At the injector face are quadlet (four-element) fuel/oxidizer injection sites and rows of round orifices (on each side of the baffles) that splash a fuel film on the baffles for convective cooling. At the end of each baffle are rows of elements that inject oxidizer (radially and axially) to react with the coolant fuel. Figures 3 will be referred to later when interpreting the shape of the data in comparison to the engine's features.

After the laser beam crossed the Titan exhaust (subassembly 2), it impinged on a beam stop located behind the engine, at the rear of the G-2 stand. The beam stop also served as a convenient visualization tool. The black-anodized, aluminum plate was painted with a fluorescent, refractory coating and index lines for spatial reference. The fluorescent coating transformed the short-duration (40-ns), ultraviolet (248-nm), invisible laser beam pulse into a relatively long-duration (milliseconds), and visible (broadband fluorescence centered at about 550 nm) spot. During an engine test, a video camera with a 532-nm bandpass filter recorded real-time measurements of the laser beam location at the beam stop.

The fluorescence imaging lens was mounted 10.67 m from the engine exhaust at right angles to the laser beam (±1 deg). The ICCD camera (Princeton Instruments Model ICCD 576) had a pixel format of 384 × 576. A UV Nikkor camera lens (focal length of 105 mm, f/4.5) was used for light collection, at a magnification M of 0.01. The camera's intensifier gate width was set for 120 ns and centered over the 40-ns laser pulse. The extra integration time allowed for jitter in the synchronization between the laser pulse and the camera gate. A closed-loop, chilled-water bath kept the detector at −35° C. To selectively capture fluorescence while blocking other light (scattered laser light at 248 nm, emission from the exhaust plume, ambient light), two filters were mounted in front of the camera lens: a bandpass filter centered at 297 nm with a FWHM of 10 nm and a UG-11 Schott glass filter to block the 445-nm second transmission band of the bandpass filter. A mechanical shutter on the camera controlled the exposure time for each image acquired; the number of laser pulses integrated in a single image was the exposure time (see Table 1) times the laser repetition rate (80 Hz). A number of images were captured at each position of the laser beam. Remote camera control and transfer of image data for storage were accomplished by a fiber optic link from the camera controller to the image acquisition computer in the G-zone control room.

The image acquisition computer was triggered 10 s before the fire switch 1 (FS-1) control room signal that started the engine and initiated the program that scanned the laser beam to the different

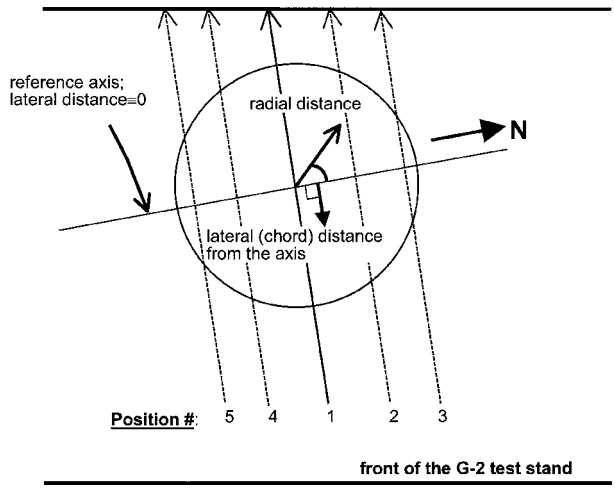

Fig. 3a Schematic of the five positions that the laser was scanned to during the engine tests.

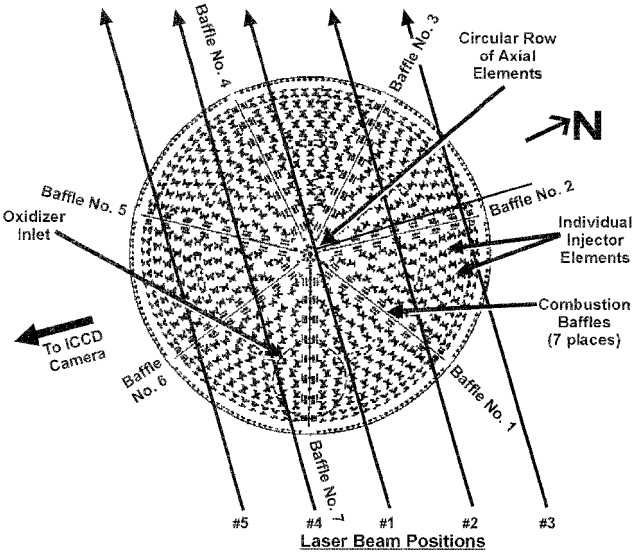

Fig. 3b Schematic of the engine injector (from below) with the laser positions also shown.

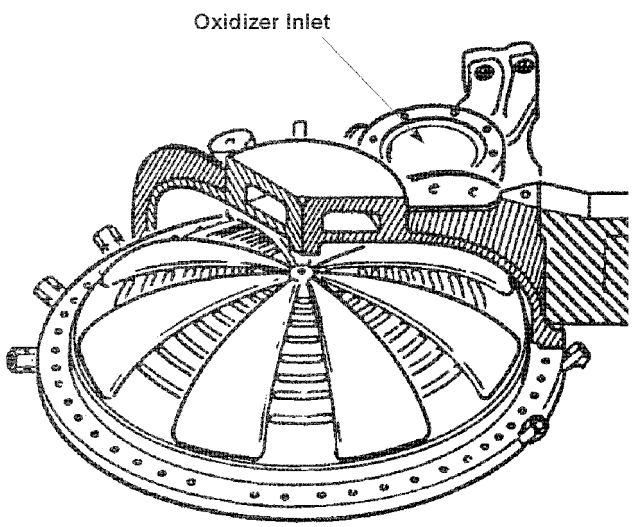

Fig. 3c Schematic detail of the oxidizer inlet.

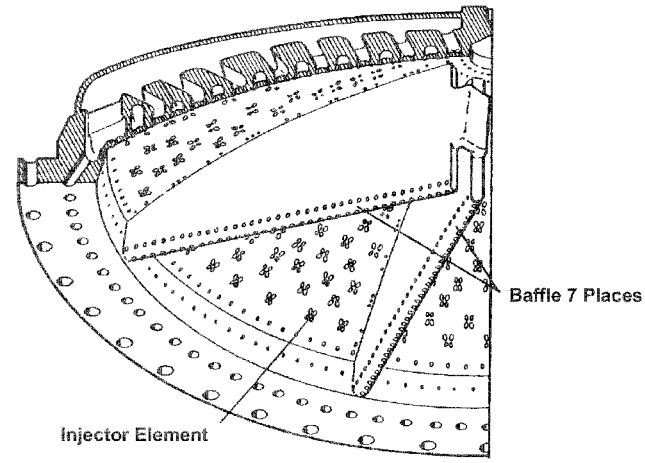

Fig. 3d Schematic detail of the of the baffles and injector (from below).

positions. The data acquisition computer in the MDL recorded FS-1, fire switch 2 (FS-2) (FS-2 ends the engine test), camera exposure time, laser grating position and PMT output, at 2000 Hz.

Measurements

This section presents the LIF results obtained with the firing Titan IV, stage I engine. For each of the tests, the chamber pressure P_c and thrust chamber MR were measured during the test. Table 1 shows the nominal conditions for each of the three tests. The thrust chamber MR includes the propellant used for fuel film cooling of the chamber wall; this is about 10% of the total fuel flow rate. The laser repetition rate (80 Hz), laser voltage (22 kV), camera position and focus, camera filters, and intensifier gate width (120 ns) were kept constant. Because the expected OH concentration increased with increasing MR, the camera exposure time was changed for each test to keep the signal within the 14-bit range of the detector. The laser energy varied between tests due to the changing conditions of the laser fill gases, as shown in Table 1.

For all tests, the laser spot was centered between 2 and 9 cm below the nozzle exit, as measured from the end of the nozzle at the north side of the engine (with the engine inclined at 2 deg, the north side is the lowest one) to the center of the burn spot (1.35 ± 0.05 cm wide by 3.05 ± 0.05 cm high). The lateral distances to the laser spots, measured horizontally from the center of the engine to the center of the burn spot, were (to ± 1 cm): 1 cm (position 1), 21 cm (position 2), 39 cm (position 3), -19 cm (position 4), and -38 cm (position 5). FLUENT code[11] predictions of the plume flowfield (with frozen chemistry) showed that the temperature and pressure fields, for standard engine conditions ($P_c = 5.91 \times 10^6$ N/m^2, MR $= 1.90$), were constant to within 10% over a vertical distance of approximately 5 cm. Because, as will be shown later, 10% variations were well within the uncertainty of the data we averaged the data over this spatial dimension.

In test 1, a checkout test, the laser wavelength was set to the on-peak wavelength and was not changed during the test. The raw data (not shown) at each position were similar over a time frame of tens of seconds, which indicated that the engine behavior was not time varying. Also, as the laser moved farther away from the centerline (position 1) the chord width of the data decreased as expected (Figs. 3a and 3b). The raw data at locations 2 and 4 were similar, as were the data at locations 3 and 5, which indicated quasi symmetry in the two halves of the engine plume.

In test 2, the laser remained was at position 1, but the laser wavelength was tuned off-peak at about 30 s into the test. Figure 4 shows the time average of all of the on-peak and off-peak data that result when the 22 rows of data are collapsed to a single row by summing the individual row's pixel values. Notice that the on-peak data are higher in magnitude because they include both the signal and background. The data presented are the average of 13 frames acquired first with the laser on-peak and then with the laser off-peak.

In test 3, the laser was scanned to the five positions while the wavelength was on-peak. Then, the wavelength was moved off-peak, and

the laser was again scanned to the five positions. Along the diameter (position 1), 12 frames of CCD camera image data were acquired, and then 2 frames each at positions 2, 3, 4, and 5. The data presented are, at position 1, the average of the 12 frames acquired, and, at positions 2, 3, 4, and 5, the average of the 2 frames captured at each of those positions.

Data Reduction

To reduce the raw data (counts vs pixel number) to the final form (MR vs position) involved three steps (Table 2).

Step 1: Raw Data

First, the abscissa in the raw data must be changed from pixel number to distance. Using an ICCD camera image of a large sign, with letters of known physical dimensions, positioned under the engine before a test determined the calibration factor of 0.218 cm/pixel. When the calibration is used, the raw data in Fig. 4 show that the fluorescence signal at position 1 extends to 0.897 m. The region of rapidly decreasing signal in the fuel film-cooling/jet boundary/shear layer expands the overall data width to 1.026 m. Because the engine nozzle's inside diameter is 0.95 m, the film cooling/boundary/shear layer must be about 6.35 cm thick, with approximately a 2.54-cm-thick layer inside the nozzle and 3.81 cm outside the nozzle.

Table 2 Summary of steps in the data reduction

Data type	Data processing steps
Raw	1) Sum image columns to obtain one-dimensional plots. 2) Calibrate the lateral position.
Corrected	1) Grating shift: multiply on-peak data by correction factor. 2) Pressure distribution: divide both on- and off-peak data by the position-dependent average pressure distribution in Fig. 5. 3) Subtract the off-peak data from the on-peak data.
Mole fraction and MR	1) Convert counts to OH mole fraction using calculated and measured values of the physical and experimental parameters in Table 3. 2) Convert mole fraction to MR using the ODK code predictions in Fig. 1.

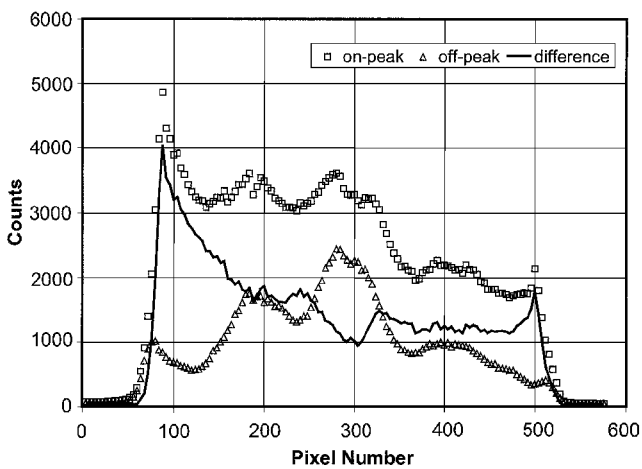

Fig. 4 Time-averaged test 2 raw data (at position 1).

Step 2: Corrected Data

To transform the one-dimensional plot of raw data into corrected data, corrections accounting for grating shift and pressure distribution were applied.

The grating shift correction was made as follows. At engine ignition, an acoustic pressure wave and a ground shock were generated that impacted the MDL and caused the laser grating (wavelength) to jump to a different location. The grating jump moved the laser wavelength off line center, which resulted in a reduction in the reference fluorescence signal. Comparison of this decreased fluorescence value to the original pretest value yielded a multiplicative correction factor, 1.27 for test 2 and 1.30 for test 3, to apply to the on-peak data. The off-peak data, by definition, did not have to be corrected for grating shift.

The pressure distribution correction was made as follows. Radial pressure variations in the flowfield will linearly affect the fluorescence signal [Eq. (2)]. The pressure distribution affects both the on-peak and off-peak data. We relied on TDK predictions of the pressure to normalize out this pressure dependence. Figure 5 shows a TDK prediction of the pressure profile for the limiting cases of MR during these tests; the dominant effect on pressure is position, rather than MR. The correction was made by dividing the raw data at each point by the average pressure at that location, as shown in Fig. 5, independent of the MR at each point. The maximum error incurred in using the average is $\pm 12\%$. Because the TDK calculations only extend to the inside edge of the nozzle, a radial distance 18.7 in. from the axis, the reduced data are truncated there.

After accounting for the described corrections, the off-peak data are subtracted from the on-peak data. The corrected data for tests 2 and 3 (position 1 only) are shown in Fig. 6. Notice that the corrections have flattened the profiles considerably, primarily due to the correction for the pressure distribution. Several qualitative observations are now possible.

1) There is higher fluorescence in the film-cooling layers (the mixing region between cold, fuel-rich gases and the cold ambient air) relative to the nearby flow. Considering the fuel film only, the fluorescence should be very low, due to low temperature and low concentration of OH (due to low MR). However, mixing of the plume with the entrained surrounding air would allow afterburning and increased OH fluorescence signal. At one point, we had used an intensified video camera, with a bandpass filter centered at 307 nm, to capture images of OH thermal emission. The images showed that the plume was particularly intense at the left edge.

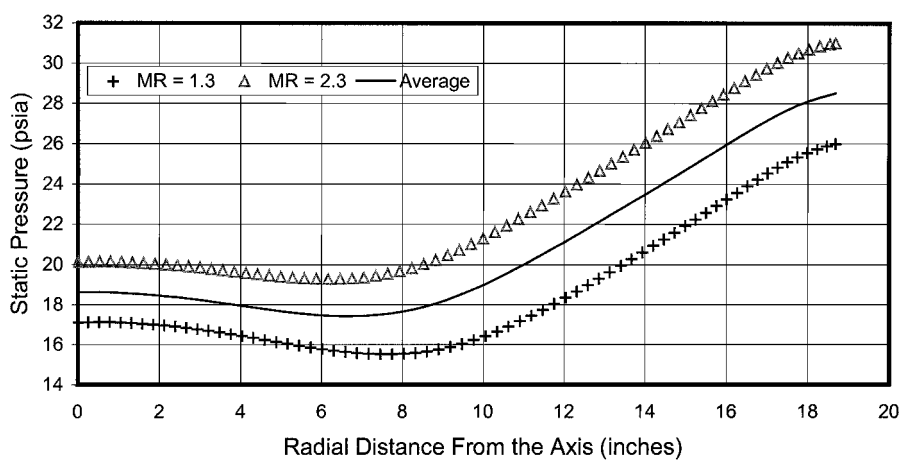

Fig. 5 TDK prediction of the static pressure profiles at the exit plane.

Table 3 Physical and experimental values needed to convert the corrected data to OH concentration

Parameter	Value	Uncertainty, %	Units	Source
η	0.516	±30 (E)[a]	Counts/photon	Calculations [$(\eta_{\text{filters}} = 0.08) \times (\eta_{\text{lens}} = 0.93) \times (\eta_{\text{camera}} = 6.93)$]
$\Omega/4\pi$	$2.9E-07$	±10 (M)[b]	——	Calculations [(1/16)(lens diameter/lens-to-plume distance)^2]
B_{12}/c	$2.2E+11$	±20 (E)	cm^2/J-s	Literature values (see Appendix)
E	0.180 (test 2) 0.185 (test 3)	±25 (M)	J/pulse	Measurements (see Table 1)
N_p	40 (test 2) 12 (test 3)	±0 (M)	Pulses	Measurements (see Table 1)
V_{pp}/Aa	0.016	±5 (M)	cm	Calculations [(22 μm pixel height) (22 μm pixel width)/ laser sheet height/M^2]
A/Q_{pre}	$4.59E-05$	±50 (E)	——	Literature values (see Appendix)
$N_T \propto k^{-1}$	$7.24E+20$	——	K/N-cm	k is Boltzmann's constant
P	0.69	±12 (E)	(N/cm^2)/psi	Distribution accounted for in the pressure correction (see Fig. 5)
$f_{\text{Br}}(T)/T$	$2.65E-05$	±10 (E)	1/K	FORTRAN model with T (from TDK) = 1300 − 2100 K
$f_{Be}(T) \times f_{Bv}(T)$	0.95	±10 (E)	——	FORTRAN model with T (from TDK) = 1300 − 2100 K
$g(\nu)$	$4.24E-11$	±10 (E)	s	FORTRAN model
Overall values	$9.28E+04$ (test 2) $2.86E+04$ (test 3)	±70	Counts/(mole fraction-psi)	

[a] E = estimated uncertainty. [b] M = uncertainty obtained from measurements.

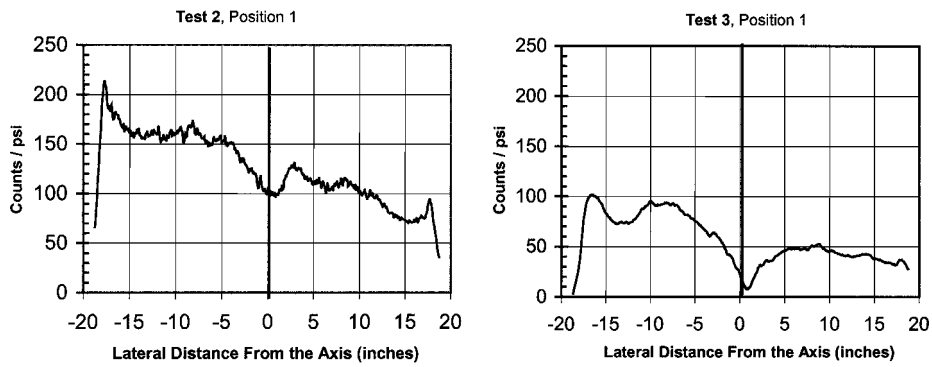

Fig. 6 Corrected data for tests 2 and 3 (at position 1).

2) There is higher signal in the left-hand half of the engine (where the laser enters the flow), with a quasi-monotonic decrease of signal from the left to the right. There are two possible explanations for this. First, because the oxidizer inlet is near the laser entry point into the plume (see Figs. 3b and 3c), it might bias the MR (and OH concentration) toward higher values, with the bias decreasing farther from the baffle. In fact, previous measurements of the oxidizer manifold pressures indicated that there could be about a 14% increase in oxidizer flow near the inlet, compared to the diametrically opposite position. Second, absorption could reduce the laser energy as the beam passed through the plume, reducing the fluorescence. This issue will be discussed in the section on error analysis.

3) The data at test 3 are qualitatively very similar to test 2, but in test 3 the region of low MR at the axis is quite pronounced. This is because in test 2 the position of the laser at position 1 was unintentionally offset 2.1 cm vs 0.6 cm in test 3, preventing the beam from passing directly through the diameter of the engine. The test 3 data more clearly reflect the circular row of injector elements at the center of the engine that feed fuel in a purely axial manner (Fig. 3b), resulting in a lower MR at the axis of the engine.

The data in Fig. 6 are linearly proportional to OH mole fraction [Eq. (1)]. We, therefore, proceed further to reduce the corrected data to OH mole fraction and local MR to estimate the magnitude of the MR fluctuations in the flow (which was the goal of this effort). Although we introduce more uncertainty in the data reduction during the further processing, we will account for the uncertainties later to bound the results.

Step 3: Mole Fraction and MR Data

To convert the corrected fluorescence signal to OH mole fraction we need to know the value of experimental constants η, Ω, and V_{pp}/Aa, physical constants B_{12}/c and A/Q_{pre}, and variables E, N_p, f_B, and $g(\nu)$ shown in Eq. (1). Table 3 shows the values we used. The results are shown in Fig. 7 for tests 2 and 3 (position 1 only). All of the test 3 data were smoothed as follows: smoothed data at point i = (1 − factor)(data at point i) + (factor)(smoothed data at point $i-1$), where the factor was 0.85. This helped to damp out the shot noise fluctuations in the data, which were as high as ±11% (see the error analysis later). Notice that the OH mole fractions in test 3 are about twice that of test 2, as expected, due to the higher MR in test 3 (Table 1).

To relate the OH mole fraction to local MR we used the ODK kinetics model (Fig. 1). We tested the sensitivity of OH variation with MR, predicted by the ODK model, using newer constants from Chemkin for four of the seven reactions that involve OH. (In the other three reactions, the rate constants in ODK were the same as available in Chemkin.) The resulting OH vs MR values were essentially the same as with the older kinetic rates. In the region (Fig. 1) between MR of 1.5 and 2.1, the plot of MR vs log(OH) is a straight line (correlation coefficient = 0.999), given by MR = 0.347[log(OH)] + 2.9166. When this relation is used, the OH mole fractions are transformed to MR. The results (including all positions from test 3) are shown in Figs. 8. Several qualitative observations are now possible:

1) The test 2 data generally lie between MR of 1.85 and 1.95, or about 6% below the average core MR for this test of 2.03 (Table 1). This agreement is surprisingly good.

2) Because the slope of the OH vs MR curve (Fig. 1) is constant between MR = 1.5 and 2.1, the MR differences across the data (Fig. 8) are independent of the absolute OH values. There is about a 0.15 MR units spread between the highest and lowest parts of the data (ignoring the edges). The ODK calculations indicate about 1.5 s of I_{sp} loss when the MR drops from 2.00 to 1.85, which, over the entire engine, would translate into a significantly decreased payload

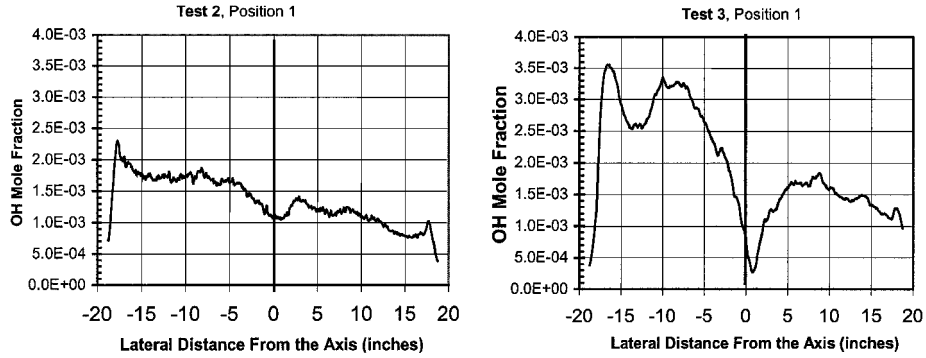

Fig. 7 OH mole fraction for tests 2 and 3 (at position 1).

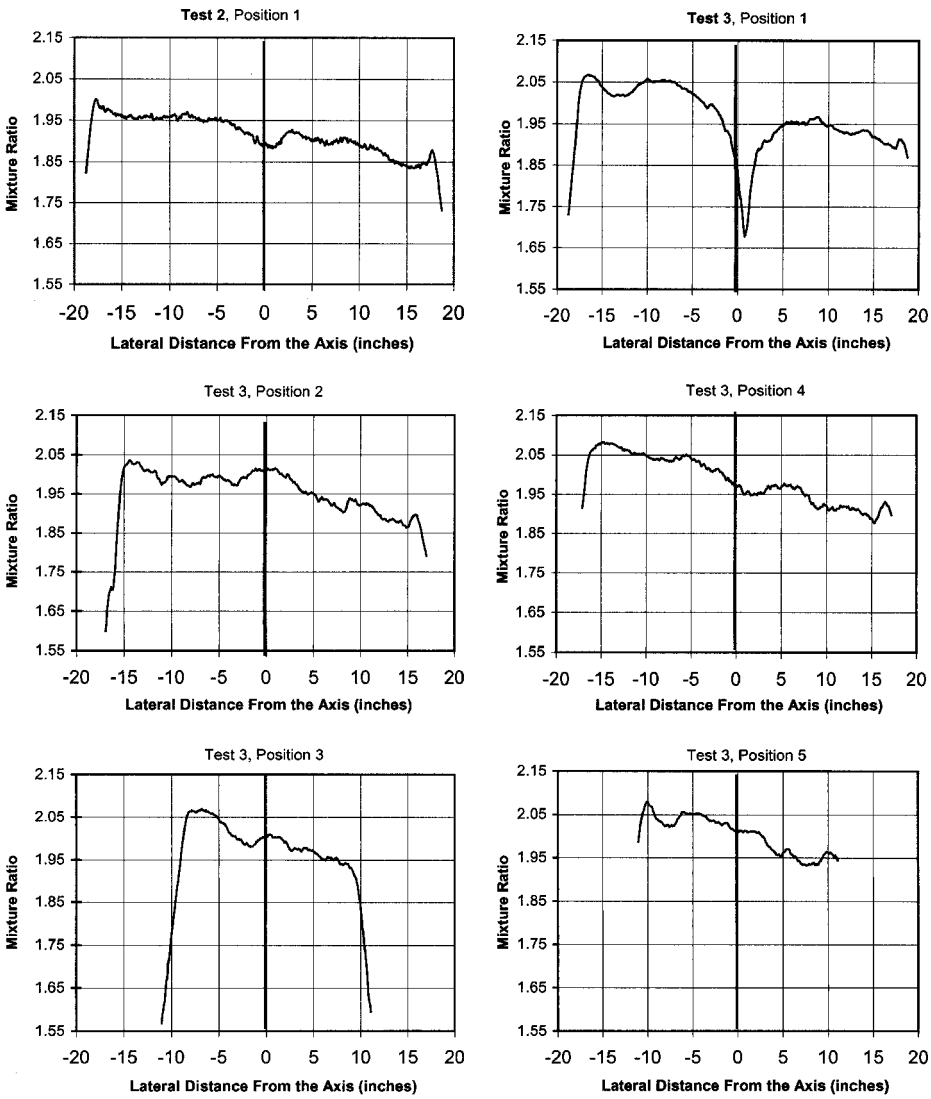

Fig. 8 Calculated MR for tests 2 and 3 (all positions).

capacity of about 771 kg or 17% of a standard Titan IV vehicle's lift capacity to geosynchronous Earth orbit.

3) The test 3 data generally lie between MR of 1.87 and 2.05, or about 16% below the average core MR for this test of 2.32. This agreement is surprisingly good.

4) In test 3, there is a deep MR depression at position 1, where the laser crossed the centerline of the engine. Because at the center of the injector is a circular row of elements that feed fuel in a purely axial manner (Fig. 3b), the depression in the data suggests that the extra fuel film cooling there is not mixing in completely with the surrounding core injector flow.

5) When crossing underneath a baffle, the MR drops by about 0.05 units. This drop (or valley) is probably caused by the laser beam passing through excess, unreacted fuel film that washes off the trailing edge of the baffles (see Fig. 3d) and lowers the local MR. For example, a valley is particularly evident near the axis in the data of test 3 at position 3 (Fig. 8). As Fig. 3b shows, when the laser is at position 3, it crosses underneath baffle 2 about halfway through

the plume. Similarly, at the other positions, the valleys correspond to the laser passing under the flow originating at the baffles.

Error Analysis

The error analysis considers noise in the signal measurement and uncertainty in the data processing used to calculate MR from the raw data. The analysis generates both relative and absolute error bars.

Noise

The noise in the measurements is from shot noise in the detector. This Poisson-distributed noise results in identical input signals being recorded differently due to the varying shot noise generated by the photocathode. The signal-to-noise ratio S/N is

$$S/N = [N_c\eta/K)]^{\frac{1}{2}} \tag{3}$$

In our case, N_C is between 1000 and 5000, η (camera quantum efficiency only) is 0.11, and K is 1.4. Therefore, the S/N is between 9 and 20, or the noise is from ±5 to ±11% of the signal. As a conservative estimate, the shot noise can be taken as ±11% throughout. Because smoothing was used on the test 3 data, averaging out the noise, the remaining small bumps in the data (Figs. 6 and 7) are fluctuations in the flow. The data in Fig. 8 are even smoother because of the logarithm processing used to get MR.

Uncertainty

Four factors are necessary to address uncertainty in the data reduction: 1) uncertainty in the values used in Table 3 (uncertainties are shown in Table 3), 2) Doppler shift correction, 3) absorption correction, and 4) saturation.

The Doppler shift correction, is addressed as follows. A shift in the absorption line position is caused by the component of the OH molecule's velocity that is in the direction of the laser beam. The absorption is reduced as the laser ends up probing farther away from line center. The Doppler shift $\Delta\omega$ is given by

$$\Delta\omega\,(\mathrm{cm}^{-1}) = (u_{\mathrm{radial}}/c)\omega \tag{4}$$

The radial velocity is strongly position dependent (Fig. 9) and not very MR dependent, and so this correction can be applied to the fluorescence data at each radial point independent of the MR. Figure 10 shows that there is very little difference between the Doppler shift at the two limiting cases of MR. Because the absorption line width is between 0.67 and 0.72 cm^{-1}, the effects of the (up to) 0.13 cm^{-1} Doppler shift on the line width are minimal. There is only a 10% decrease in absorption at the periphery compared to the absorption at the center of the plume.

After the grating shift off line center, however, the Doppler shift and resulting absorption change are no longer symmetric about the engine axis. On the front half of the engine (the left half of the data) the Doppler shift back toward line center would cause an increased absorption of about 20%, using the worst case of a 0.13 cm^{-1} Doppler shift (Fig. 10). On the back half of the engine (the right half of the data), where the sign of the radial velocity changed, a decrease of about 25% would occur. We, therefore, estimated the Doppler shift correction to apply (after already applying grating shift correction earlier) as −20% at the left edge of the data, 0% at the axis, and +25% at the right edge (Table 4).

Next is the absorption correction. We estimated the magnitude of laser absorption using ODK predictions of the flowfield temperature, pressure and OH concentration, and synthetic OH absorption spectra (FORTRAN code) that were convolved with the laser bandwidth. Using the line center value of the absorption coefficient (a worst case), we calculated absorption across the full 0.95-m plume diameter (a worst case) assuming absorption according to Beer's law.

Table 4 Overall relative and absolute errors in the OH mole fraction and MR

Noise or uncertainty	Relative (locally)	Relative (globally)	Absolute
Shot noise	Include	Include	Include
Doppler shift uncertainty	——	Include	Include
Absorption uncertainty	——	Include	Include
Saturation uncertainty	——	Include	Include
Values uncertainty (Table 3), %	——	±12	±70
[OH] overall error, % (applies to the data of Fig. 7)	−11, +11 throughout the flow	−23, +61 (L)[a] −12, +62 (C) −12, +71 (R)	−73, +92 (L) −70, 93 (C) −70, +99 (R)
MR overall error, % (applies to the data of Figure 8)	−1, +1 throughout the flow	−2, +6 throughout the flow	−11, +7 throughout the flow

[a]L = left edge of the flow; C = center; R = right edge of the flow.

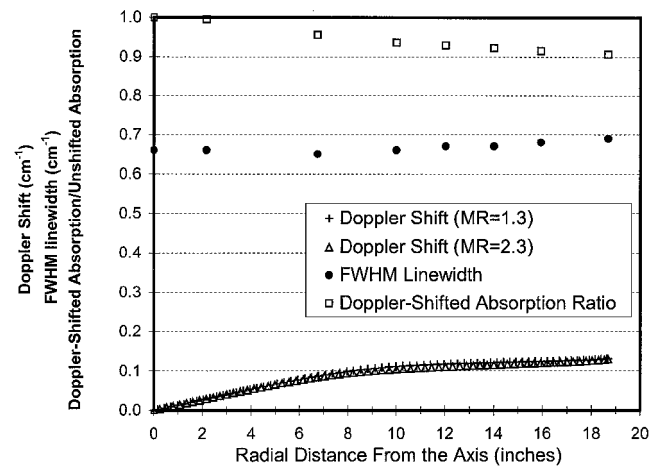

Fig. 10 Calculated Doppler shift, absorption line width (FWHM), and Doppler-shifted absorption ratio.

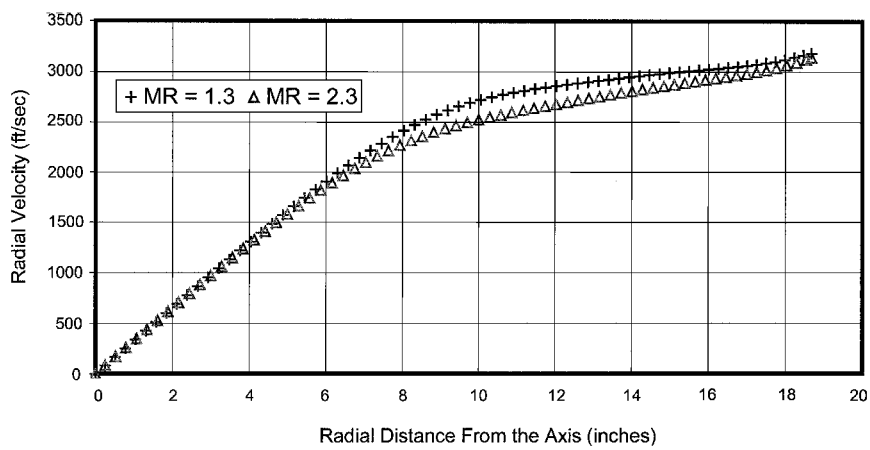

Fig. 9 TDK prediction of the radial velocity profiles at the exit plane.

Table 5 Estimate of laser absorption

MR	ODK static pressure, atm	ODK static temperature, K	ODK OH mole fraction	Line center absorption coefficient, cm^{-1} atm^{-1}	Laser intensity at 0.95 m (relative to I_0)
1.4	1.31	1513	3.87E−05	0.21	1.00
1.6	1.37	1707	1.64E−04	0.21	1.00
1.8	1.44	1893	6.40E−04	0.20	0.98
2.0	1.52	2070	2.30E−03	0.19	0.94
2.2	1.59	2178	7.07E−03	0.19	0.82
2.4	1.58	2156	9.70E−03	0.19	0.76
2.5	1.57	2120	9.82E−03	0.19	0.76
2.6	1.57	2084	9.55E−03	0.19	0.76

Table 5 shows the values used. Then, for the correction to the data, we used a linear estimate of the calculated absorption: 0% at the left edge of the data (where the laser has just entered the plume), +12% at the axis, and +24% at the right edge.

Last is saturation. We calculated the saturation energy at about 120 mJ (conservative). Because the laser energy was about 180 mJ (Table 1), the fluorescence signal (proportional to $E/[1+E/E^{sat}]$) could have been reduced by as much as 60% because of saturation. The uncertainty is, therefore, +60% across the data.

The total relative error in the data (between nearby pixels) is only a function of the shot noise in the measurements. The total relative error across larger distances in the flow is a function of the shot noise and uncertainties in the pressure correction (Table 3), Doppler shift, absorption, and saturation. The total absolute error is a function of the shot noise in the measurements and all of the uncertainties just discussed. When the error sources are independent (or uncorrelated), the errors are calculated by summing over the individual errors as

$$\text{total error} = \sqrt{\left[\sum_i (\text{error}_i)^2\right]} \tag{5}$$

Table 4 summarizes the results. The absolute errors in the OH mole fraction are between −73% and +99%, and the absolute errors in MR are between −11% and +7%. Notice that the absolute errors at the left edge, center, and right edge of the flow are roughly the same. Then, more important, the overall absolute errors do not bias the shape of the MR curves from their appearance in Fig. 8. Also, because the relative (locally) errors in MR are very small (±1%), the valleys in the data are from actual nonuniformities in the flow.

Remaining uncertainty about the effect of absorption could be addressed in the future with a dual-direction approach, whereby the laser crosses the flow in parallel but opposing directions. One implementation of this yields the true scalar flowfield, corrected for absorption, with the only requirement that the absorption behaves linearly, i.e., according to Beer's law.[12]

Conclusions

The laser experiments provided (inferred) measurements of OH concentration and MR in the exit plane of a firing Titan IV rocket engine. The measurements showed that there is a consistent trend in MR distribution across the engine that persists at different engine operating conditions, such that closer to the oxygen inlet the MR is higher. Also, the MR was seen to decrease underneath baffles by about 0.05 MR units. Absorption of the laser beam, and other uncertainties, was not enough to explain these trends.

As mentioned earlier, nonuniformities in the MR profile could cause a decrease in engine performance. Improvements could result from small modifications to the engine injector or baffle cooling. These changes might include radially injecting some oxidizer (N_2O_4) from the baffle tips toward the fuel film-cooled injector axis, adjusting the fuel film cooling of the baffles, and adding a screen to improve distribution of the oxidizer.

One of the shortcomings of these experiments was the lack of a calibration to reduce the uncertainty in the data reduction. In the future, Raman scattering from N_2 at the test stand, or LIF of OH from our reference burner placed temporarily underneath the engine exit, would be appropriate choices for calibration. The initial ignition transient of the engine caused a pressure/vibration transient that caused the laser grating to jump to a new position, that is, new laser wavelength. This uncontrolled movement of the grating is undesirable and should be avoided in the future by better shock mounting of the laser and/or the grating. The laser energy should also be reduced to avoid saturation and to prevent the complicating effects of rotational energy transfer (see the Appendix).

Appendix: Spectroscopy Details

A/Q_{pre}

$A_{v'=3}$ has been reported as 8.21×10^5 s^{-1} (for $N'=11$) (Ref. 13) and 1.1×10^6 s^{-1} (no N' indicated).[6] Using an average of the two, and the ratio $A_{3,2}/A_{v'=3}$ of 0.64 (Ref. 9), results in $A_{3,2}=6.1\times10^5$ s^{-1} . Q_{pre} has been reported as 1.33×10^{10} s^{-1} (for $N'=11$) (Ref. 13). Therefore, $A/Q_{pre}=4.59\times10^{-5}$.

B_{12}/c

B_{12}/c has been reported as 1.2×10^{11} cm^2/J-s for pumping $P_1(8)$ (3,0) (Ref. 6). For $Q_2(11)$, $J''=10.5$ and $2J''+1=22$; for $P_1(8)$, $J''=8.5$ and $2J''+1=18$. Using published rotational transition probabilities,[9] we find $[S_{Q2(11)}/22]/[S_{P1(8)}/18]$ is 1.87. Therefore, for $Q_2(11)$, B_{12}/c is 2.2×10^{11} cm^2/J-s.

Energy Transfer

We avoided complications from vibrational energy transfer of the $v'=3$ state to nonpredissociating vibrational levels by optically filtering to collect only $v'=3\rightarrow v''=2$ fluorescence. Although we used predissociative fluorescence to remove the impact of collisions on the signal, rotational energy transfer (RET) could restore dependence on collisions. It is known that temperature measurements are impacted by RET.[14] As long as less than about 20% of the ground state rotational level's population is removed by a single laser pulse, then RET is unimportant.[15] With our high laser intensities, we probably introduced some dependence on quenching collisions, and as an approximation, we take the quenching to vary linearly with pressure and collision cross sections and inversely with the square root of temperature. TDK shows that the pressure, temperature, and cross sections are not strongly dependent on MR in our tests. Because the dominant factor on quenching is pressure, we use Fig. 5 to estimate that the collisional quenching term would decrease slightly from the center outward, then rise by about a factor of about 1.5 toward the edge of the plume. Although determining the exact amount of this quenching is beyond the scope of this paper, accounting for quenching in the data reduction would have increased the OH mole fraction and MR toward the the edges of the plume. This would not affect any of the conclusions stated in this paper.

Acknowledgments

This work was funded by Lockheed Martin Astronautics subcontract to U.S. Air Force Contract F04701-85-C-0019 for Titan Continuous Product/Process Improvement. Cherie Cotter at Aerojet was responsible for the One-Dimensional Kinetics and Two-Dimensional Kinetics calculations, and for relating mixture ratio (MR) to I_{sp}. Ross Hewitt helped relate the MR trends in the data to the injector's physical characteristics.

References

[1] Sutton, G. P., *Rocket Propulsion Elements,* 5th ed., Wiley, New York, 1986, p. 136.

[2] Brasier, C. W., Porter, R. G., Anspach, K. M., Simmons, M. A., Wallace, T. L., and Cobb, S. H., "Results of Laser-Induced Fluorescence Measurements on OMS Shuttle Engine," 20th JANNAF Exhaust Plume Technology Subcommittee Meeting, Feb. 1993.

[3] Williams, D. R., McKeown, D., Porter, F. M., Baker, C. A., Astill, A.G., and Rawley, K. M., "Coherent Anti-Stokes Raman Spectroscopy (CARS) and Laser-Induced Fluorescence (LIF) Measurements in a Rocket Engine Plume," *Combustion and Flame*, Vol. 94, 1993, pp. 77–90.

[4] Nickerson, G. R., Berker, D. R., Coats, D. E., and Dunn, S. S., "Two-Dimensional Kinetics (TDK) Nozzle Performance Computer Program," Software and Engineering Associates, Inc., NAS8-39048, 31 March 1993.

[5]Quagliaroli, T. M., Laufer, G., Krauss, R. H., and McDaniel, J. C., Jr., "Laser Selection Criteria for OH Fluorescence Measurements in Supersonic Combustion Test Facilities," *AIAA Journal*, Vol. 31, No. 3, 1993, pp. 520–527.

[6]Seitzman, J. M., and Hanson, R. K., "Comparison of Excitation Techniques for Quantitative Fluorescence Imaging of Reacting Flows," *AIAA Journal*, Vol. 31, No. 3, 1993, pp. 512–519.

[7]Andresen, P., Schlüter, H., Wolff, D., Voges, H., Koch, A., Hentschel, W., Opperman, W., and Rothe, E., "Identification and Imaging of OH ($v'' = 0$) and O_2 ($v'' = 6$ or 7) in an Automobile Spark-Ignition Engine Using A Tunable KrF Excimer Laser," *Applied Optics*, Vol. 31, No. 36, 1992, pp. 7684–7689.

[8]Quagliaroli, T. M., Grinstead, J. H., Laufer, G., Krauss, R. H., Whitehurst, R. B., and McDaniel, J. C., Jr., "Planar OH Density and Apparent Temperature Measurements in a Supersonic Combustion Flow," AIAA Paper 95-0512, Jan. 1995.

[9]Andresen, P., Bath, A., Gröger, W., Lülf, H. W., Meijer, G., and Ter Meulen, J. J., "Laser-Induced Fluorescence with Tunable Excimer Lasers as a Possible Method for Instantaneous Temperature Field Measurements at High Pressures," *Applied Optics*, Vol. 27, No. 2, 1988, pp. 365–378.

[10]Gray, J. A., and Farrow, R. L., "Predissociation Lifetimes of OH $A^2\Sigma^+(v' = 3)$ Obtained From Optical–Optical Double-Resonance Linewidth Measurements," *Journal of Chemical Physics*, Vol. 95, No. 10, 1991, pp. 7054–7060.

[11]FLUENT User's Guide, Ver. V4.2, Fluent Inc., Jan. 1993.

[12]Talley, D. G., Verdieck, J. F., Lee, S. W., McDonell, V. G., and Samuelsen, G. S., "Accounting for Laser Sheet Extinction in Applying PLLIF to Sprays," AIAA Paper 96-0469, Jan. 1996.

[13]Heard, D. E., Crosley, D. R., Jeffries, J. B., Smith, G. P., and Hirano, A., "Rotational Level Dependence of Predissociation in the $v' = 3$ Level of OH $A^2\Sigma^+$," *Journal of Chemical Physics*, Vol. 96, No. 6, 1992, pp. 4366–4371.

[14]Rothe, E. W., Gu, Y., Chryssostomou, A., Andresen, P., and Bormann, F., "Effect of Laser Intensity and of Lower-State Rotational Energy Transfer Upon Temperature Measurements Made With Laser-Induced Predisssociative Fluorescence," *Applied Physics B*, Vol. 66, 1998, pp. 251–258.

[15]Rothe, E. W., and Andresen, P., "Application of Tunable Excimer Lasers to Combustion Diagnostics: a Review," *Applied Optics*, Vol. 36, No. 18, 1997, pp. 3971–4033.

R. P. Lucht
Associate Editor